Downloaded from https://www.cambridge.org/core. University of Basel Library, on 30 May 2017 at 17:27:58, subject to the Cambridge Core terms of use, available at https://www.cambridge.org/core/terms. https://doi.org/10.1017/jfm.2014.229

J. Fluid Mech. (2014), *vol.* 749, *pp.* 519–541. © Cambridge University Press 2014
doi:10.1017/jfm.2014.229

Scale analysis of miscible density-driven convection in porous media

Patrick Jenny[1,†], Joohwa S. Lee[1], Daniel W. Meyer[1] and Hamdi A. Tchelepi[2]

[1]Institute of Fluid Dynamics, ETH Zurich, Sonneggstrasse 3, 8092 Zurich, Switzerland

[2]Department of Energy Resources Engineering, Stanford University, Stanford, CA 94305, USA

(Received 2 May 2013; revised 9 April 2014; accepted 19 April 2014;
first published online 16 May 2014)

Scale analysis of unstable density-driven miscible convection in porous media is performed. The main conclusions for instabilities in the developed (long time scales) regime are that (i) large-scale structures are responsible for the bulk of the production of concentration variance, (ii) variance dissipation is dominated by the small (diffusive) scales and that (iii) both the production and dissipation rates are independent of the Rayleigh number. These findings provide a strong basis for a new modelling approach, namely, large-mode simulation (LMS), for which closure is achieved by replacing the actual diffusivity with an effective one. For validation, LMS results for vertical flow in a homogeneous rectangular domain are compared with direct numerical simulations (DNS). Some of the analysis is based on the derivation and closure of the concentration mean and variance equations, whereby averaging over the ensemble of all possible initial perturbations is considered. While self-similar solutions are obtained for vertical, statistically one-dimensional fingering, triple correlation of concentration and scalar dissipation rate (rate at which the concentration variance decays due to diffusion) have to be modelled in the general case. For this purpose, an ensemble-averaged Darcy modelling (EADM) approach is proposed.

Key words: buoyancy-driven instability, convection in porous media, fingering instability

1. Introduction

Geologic sequestration of carbon dioxide is one of the most promising technologies for reducing CO_2 emissions. After capturing the CO_2 (e.g. from fossil-fuel-based power plants), it is injected into suitable subsurface formations at depths greater than approximately 800 m. At such depths, the CO_2 is in a supercritical state, which has a liquid-like density and a gas-like viscosity (see Holloway & Savage 1993; Yang & Gu 2006). For the geologic storage of carbon dioxide, saline aquifers are considered because of their high storage capacity. The supercritical CO_2 is expected to be immiscible with, and less dense than, the brine in the aquifer. As a result, the injected CO_2 tends to form a plume that overrides the brine and rises upward until it reaches the top of the aquifer, which is assumed in the ideal case to have an impermeable caprock (see Bachu, Gunther & Perkins 1994). However, saline aquifers may not meet the ideal setting of a perfectly sealing caprock. As a result, in order to

† Email address for correspondence: pajenny@ethz.ch

employ safe CO_2 sequestration at a global scale, one has to rely on other mechanisms that lead to a permanent trapping of the injected CO_2.

An important permanent trapping mechanism is based on the dissolution of the injected CO_2 into the brinephase (IPCC 2005, figure 5.9). Here CO_2 dissolves readily in brine with a typical solubility of 5 % by volume (see Ennis-King & Paterson 2005). Since the density of brine increases monotonically with the CO_2 concentration (see Lindeberg & Bergmo 2003), then within the diffusive boundary layer, heavier CO_2-rich brine overlies brine with lower CO_2 concentrations. This unstable density stratification reaches critical conditions eventually, which lead to the onset of an instability. Thereafter, the unstable modes evolve into large-scale CO_2-rich fingers that transport significant amounts of CO_2 deeper into the formation (see Ennis-King & Paterson 2005; Ennis-King, Preston & Paterson 2005; Riaz *et al.* 2006; Farajzadeh *et al.* 2007; Kneafsey & Pruess 2010). As a result, this transport mechanism, referred to as gravity fingering, leads to permanent trapping of CO_2. Moreover, this convective transport mechanism enhances the overall dissolution rate, or mass flux, of CO_2 across the CO_2-brine interface compared with the stratified diffusion-driven case.

Miscible gravity fingering in porous media has been studied extensively. To investigate the onset time of convective flow in a diffusive boundary layer and the corresponding wavelength, linear stability analysis based on decomposition of the concentration field into a base state and a perturbation has been employed, e.g. by Ennis-King & Paterson (2005), Ennis-King *et al.* (2005), Riaz *et al.* (2006) and Pau *et al.* (2010).

However, for practical applications, it is more important to predict the long-term fate of the injected CO_2. For the subsurface formations of interest, predictions must be made using numerical simulation. Examples of high-resolution nonlinear simulations of miscible density-driven convection in homogeneous domains include Lindeberg & Bergmo (2003), Hesse, Tchelepi & Orr (2006), Farajzadeh *et al.* (2007), Pau *et al.* (2010), Ghesmat, Hassanzadeh & Abedi (2011) and Hewitt, Neufeld & Lister (2013). These studies show that the nonlinear dynamics are quite complex, and that the numbers and patterns of the fingers are all strong functions of the Rayleigh number, Ra, which quantifies the ratio of convective to diffusive transport. Moreover, these investigations, especially those of Hesse *et al.* (2006) and Pau *et al.* (2010), showed that the long-term CO_2 mass flux (integrated across the full width of the formation) is nearly constant and independent of Ra. Even though the Ra range that can be modelled accurately is limited, the findings from high-resolution numerical solutions are quite consistent with observations of miscible convection in laboratory experiments, e.g. of Slim *et al.* (2013). It is worth noting that some Ra dependence was postulated by Neufeld *et al.* (2010). In the experimental study of Slim *et al.* (2013), long-term gravity-fingering was studied in a Hele-Shaw cell with a fixed interface across which molecular diffusion takes place. In Neufeld *et al.* (2010), a fluid system with similar properties to the brine/CO_2 system was studied both experimentally and numerically and good agreement was obtained. Unlike in the set-up studied by Slim *et al.* (2013), however, no fixed dissolution interface was enforced. Hidalgo *et al.* (2012) studied gravity fingering numerically in both configurations. They analysed integral quantities like the overall dissolved CO_2 or the scalar-dissipation rate integrated over the computational domain. Like Hesse *et al.* (2006) and others, but unlike Neufeld *et al.* (2010), they found that the long-term CO_2 mass flux is independent of Ra.

The accuracy of predictions of gravity fingering depends on the ability to resolve the relevant length and time scales associated with the nonlinear finger dynamics and

Downloaded from https://www.cambridge.org/core. University of Basel Library, on 30 May 2017 at 17:27:58, subject to the Cambridge Core terms of use, available at https://www.cambridge.org/core/terms. https://doi.org/10.1017/jfm.2014.229

the size of the domain of interest, which can span extremely wide ranges. These resolution requirements on the length and time scales pose serious challenges for modelling the long-term evolution of subsurface CO_2 plumes in the planning phase of CO_2 sequestration operations. If the small-scale structures, that drive gravity fingering, which in turn enhances the CO_2 mass flux, are underresolved, the CO_2 storage capacity of potential geological sequestration sites may be underestimated; more importantly, the details of the plume distribution in space and time can be quite inaccurate. Thus, when simulating CO_2 plumes in subsurface formations at high Ra, we are faced with the challenge of developing coarse-scale approaches that capture the subscale nonlinear dynamics accurately and efficiently.

Based on the findings that (i) the time for the onset of convection is relatively short and that (ii) the CO_2 flux in the nonlinear convective regime is nearly constant over time, several investigators have proposed 'upscaling' strategies of density-driven fingering when modelling CO_2 migration in large subsurface formations, especially in the long post-injection period. Pruess & Nordbotten (2011, p. 147) employed coarse-scale numerical simulations with a subscale model based on the observation that the long-term convection-enhanced flux is constant and independent of time. The subscale model removes CO_2 artificially at the top of the simulated CO_2 plume with a constant mass flux neglecting onset dynamics. The applied mass flux was estimated based on a small-scale gravity-fingering simulation, where gravity fingers were resolved. Gasda, Nordbotten & Celia (2011) developed a vertically integrated sharp-interface numerical model for CO_2 injection and long-term migration, which accounts for residual and solubility trapping. The enhanced CO_2 solubility due to density-driven miscible convection at scales smaller than the numerical grid size is captured using a relatively simple mass-transfer model. Their model also relied on the assumptions that the instability onset time is short compared with the time scale of interest and that the dissolution rate is constant. MacMinn, Szulczewski & Juanes (2011, § 3.2) developed semi-analytical solutions of gravity currents, in which the dissolution mass flux was represented with a simple algebraic expression that was formulated based on scaling arguments.

In the simulation of CO_2 plume migration in subsurface formations, resolving the wide spectrum of scales associated with the miscible convection problem is not feasible, and there is a need for reliable models that can capture the statistical moments of the CO_2 concentration without fully resolving the fine details, i.e. gravity fingering. Here, the evolution dynamics of modes associated with different wavenumbers are discussed. Theoretical results from our scale analysis and numerical investigations are presented. These findings provide justification for a large-mode simulation (LMS) strategy whereby a coarse-scale formulation that accounts for the high-wavenumber dynamics is constructed without fully resolving the finest scales. LMS enables accurate quantification of the gravity-fingering-enhanced CO_2 mass flux without the necessity to resolve the smallest fingering structures. For our scale analysis of density-driven gravity fingering, a two-dimensional homogeneous porous formation that spans many finger widths in the horizontal direction is considered, and ergodicity in the horizontal direction is assumed. For this case, self-similar, one-dimensional profiles of ensemble-averaged quantities (such as the mean concentration and variance) can be derived.

Next, the ensemble-averaged equations are derived and discussed. In § 3, the characteristic length scales of our scale analysis and the scalar dissipation rate, which is an important quantity in the variance equation of the CO_2 concentration, are analysed. The findings lead to strong arguments in favour of our LMS approach. In

Downloaded from https://www.cambridge.org/core. University of Basel Library, on 30 May 2017 at 17:27:58, subject to the Cambridge Core terms of use, available at https://www.cambridge.org/core/terms. https://doi.org/10.1017/jfm.2014.229

§ 4, numerical investigations are presented, which show comparisons of LMS results with direct numerical simulations (DNS). The summary and conclusions are given in § 5.

2. Ensemble-averaged equations

The scale analysis presented here relies in part on the ensemble-averaged equations. They facilitate discussions not only of average (mean) concentration fields, but also of the production and dissipation of concentration variance. It will be shown that the only terms in the normalized equations that depend on the Rayleigh number are diffusion of the mean and variance of concentration and the dissipation of concentration variance. It is shown that the concentration variance evolution also depends on the concentration triple correlation, which may depend on the Rayleigh number. For very large Rayleigh numbers, the two diffusion terms become quite small and can be neglected. The Rayleigh number dependence on the triple correlation term and scalar dissipation rate must be quantified, which is the subject of the next section.

We consider incompressible miscible flow in porous media with density differences due to concentration variation, i.e.

$$\frac{\partial}{\partial x_i}\overbrace{\left(\frac{k}{\mu\phi}\left(\frac{\partial p}{\partial x_i}-\rho(C)g\frac{\partial z}{\partial x_i}\right)\right)}^{-u_i}=0 \tag{2.1}$$

$$\frac{\partial C}{\partial t}+\frac{\partial u_i C}{\partial x_i}=\frac{\partial}{\partial x_i}\left(D\frac{\partial C}{\partial x_i}\right), \tag{2.2}$$

where p is the fluid pressure, $\rho=\rho_0+C\Delta\rho$ is the fluid density with the difference $\Delta\rho$ between the heavy and light miscible fluids, μ the constant viscosity, D the diffusion coefficient, ϕ the porosity (constant), k the permeability, g the gravitational acceleration and z the depth. Here, $C\in[0,\,1]$ is the CO_2 concentration or more precisely the CO_2 concentration normalized by the CO_2 solubility. In (2.1) and (2.2), the Boussinesq approximation was adopted.

For convenience, we choose the orientation of the Cartesian coordinate system such that $\boldsymbol{x}=(x_1=x,\,x_2=y,\,x_3=z)^{\mathrm{T}}$, and we apply the transformations

$$\tilde{t}=\frac{\bar{u}}{H}t \quad\text{and}\quad \tilde{x}_i=\frac{1}{H}x_i, \tag{2.3a,b}$$

with the reference velocity

$$\bar{u}=\frac{\bar{k}g\Delta\rho}{\mu\phi}, \tag{2.4}$$

to obtain the dimensionless equations

$$\frac{\partial\tilde{u}_i}{\partial\tilde{x}_i}=0 \tag{2.5}$$

$$\frac{\partial C}{\partial\tilde{t}}+\frac{\partial\tilde{u}_i C}{\partial\tilde{x}_i}=\frac{1}{Ra}\frac{\partial^2 C}{\partial\tilde{x}_i\partial\tilde{x}_i}. \tag{2.6}$$

The Rayleigh number is defined as

$$Ra=\frac{\bar{u}H}{D}, \tag{2.7}$$

Downloaded from https://www.cambridge.org/core. University of Basel Library, on 30 May 2017 at 17:27:58, subject to the Cambridge Core terms of use, available at https://www.cambridge.org/core/terms. https://doi.org/10.1017/jfm.2014.229

where H is a macroscopic length scale and $\bar{k}$ is the average permeability. For the dimensionless velocity, one obtains

$$\tilde{u}_i = -\tilde{k}\left(\frac{\partial \tilde{p}}{\partial \tilde{x}_i} - (\rho_0/\Delta\rho + C)\frac{\partial \tilde{z}}{\partial \tilde{x}_i}\right) \tag{2.8}$$

with

$$\tilde{p} = \frac{p}{Hg\Delta\rho}, \quad \tilde{k} = \frac{k}{\bar{k}} \quad \text{and} \quad \tilde{z} = \frac{z}{H}. \tag{2.9a–c}$$

From now on, we consider homogeneous porous media with gravitationally unstable flow at large Rayleigh numbers. For such flows, each independent realization with slightly different initial perturbations leads to a different outcome. Detailed solution of the problem for a particular realization is not the objective. Instead, we are interested in the long-term concentration statistics across the ensemble of all possible realizations subject to different initial (small and random) perturbations. Next, we derive the ensemble-averaged equations for the expectation and variance of C, i.e. $\langle C\rangle$ and $\langle C'C'\rangle$, respectively, where $C' = C - \langle C\rangle$ is the perturbation around the mean. Unlike in the work of Hidalgo *et al.* (2012), where angular brackets correspond to volume averaging over the entire computational domain, in this work, angular brackets refer to averages over an ensemble of realizations with differently perturbed initial conditions.

We can formally express the expectation of a quantity F as

$$\langle F\rangle = \lim_{n\to\infty}\frac{1}{n}\sum_{j=1}^{n} F^j = \int_0^1 Ff(c)\,\mathrm{d}c, \tag{2.10}$$

where $f(c)$ is the probability density function (PDF) of C, which depends on the location $\boldsymbol{x}$ and time t. Note that C is the concentration of a realization, and c is the independent concentration sample space variable. Here, the superscript $j \in \{1, \ldots, n\}$ denotes the jth realization. Thus, we obtain

$$\langle C\rangle = \int_0^1 cf(c)\,\mathrm{d}c \quad \text{and} \quad \langle C'C'\rangle = \int_0^1 c^2 f(c)\,\mathrm{d}c - \langle C\rangle^2 \tag{2.11a,b}$$

and averaging the concentration transport equation leads to

$$\frac{\partial\langle C\rangle}{\partial\tilde{t}} + \frac{\partial\langle\tilde{u}_i C\rangle}{\partial\tilde{x}_i} = \frac{1}{Ra}\frac{\partial^2\langle C\rangle}{\partial\tilde{x}_i\partial\tilde{x}_i}. \tag{2.12}$$

Note that (2.12) follows from (2.6), relation (2.11) between moments of C and $f(c)$, and the fact that spatial, as well as temporal, derivatives commute with integration over the c-space. Multiplication of (2.6) with $2C$, and averaging leads to

$$\frac{\partial\langle C^2\rangle}{\partial\tilde{t}} + \frac{\partial\langle\tilde{u}_i C^2\rangle}{\partial\tilde{x}_i} = \frac{1}{Ra}\frac{\partial^2\langle C^2\rangle}{\partial\tilde{x}_i\partial\tilde{x}_i} - \frac{2}{Ra}\left\langle\frac{\partial C}{\partial\tilde{x}_i}\frac{\partial C}{\partial\tilde{x}_i}\right\rangle \tag{2.13}$$

and multiplying (2.12) with $2\langle C\rangle$ yields

$$\frac{\partial\langle C\rangle^2}{\partial\tilde{t}} + \frac{\partial 2\langle C\rangle\langle\tilde{u}_i C\rangle}{\partial\tilde{x}_i} = \frac{1}{Ra}\frac{\partial^2\langle C\rangle^2}{\partial\tilde{x}_i\partial\tilde{x}_i} - \frac{2}{Ra}\frac{\partial\langle C\rangle}{\partial\tilde{x}_i}\frac{\partial\langle C\rangle}{\partial\tilde{x}_i} + 2\langle\tilde{u}_i C\rangle\frac{\partial\langle C\rangle}{\partial\tilde{x}_i}. \tag{2.14}$$

Downloaded from https://www.cambridge.org/core. University of Basel Library, on 30 May 2017 at 17:27:58, subject to the Cambridge Core terms of use, available at https://www.cambridge.org/core/terms. https://doi.org/10.1017/jfm.2014.229

Subtraction of (2.14) from (2.13) leads to

$$\frac{\partial\langle C'C'\rangle}{\partial\tilde{t}}+\frac{\partial}{\partial\tilde{x}_i}\underbrace{\left(\langle\tilde{u}_iC'C'\rangle-\frac{1}{Ra}\frac{\partial\langle C'C'\rangle}{\partial\tilde{x}_i}\right)}_{\tilde{F}_i^{cc}}=-\tilde{\chi}+\tilde{\mathscr{P}}. \tag{2.15}$$

This is a balance equation for the concentration variance, $\langle C'C'\rangle$, in which the variance flux is $\tilde{F}_i^{cc}$. The scalar variance production, $\tilde{\mathscr{P}}$, and dissipation rate, $\tilde{\chi}$, are defined as

$$\tilde{\mathscr{P}}=-2\langle\tilde{u}_i'C'\rangle\frac{\partial\langle C\rangle}{\partial\tilde{x}_i}\quad\text{and}\quad\tilde{\chi}=\frac{2}{Ra}\left\langle\frac{\partial C'}{\partial\tilde{x}_i}\frac{\partial C'}{\partial\tilde{x}_i}\right\rangle. \tag{2.16a,b}$$

The corresponding dimensional counterparts for $\tilde{\mathscr{P}}$ and $\tilde{\chi}$ are

$$\mathscr{P}=\frac{\bar{u}}{H}\tilde{\mathscr{P}}\quad\text{and}\quad\chi=\frac{\bar{u}}{H}\tilde{\chi}. \tag{2.17a,b}$$

Note that in the absence of $\mathscr{P}$ and χ, the rate of variance would be balanced by the divergence of the flux of the concentration variance, $\tilde{F}_i^{cc}$.

Next, we show how transport (i.e. concentration evolution) can be decoupled from flow (i.e. pressure) based on the established observation that for our setting $|\tilde{\nabla}\tilde{p}'|\ll|\tilde{\nabla}\langle\tilde{p}\rangle|$ (see Lake 1989; Yortsos 1995; Yang & Yortsos 1997). Note that $\tilde{p}=\langle\tilde{p}\rangle+\tilde{p}'$. First, we express $\boldsymbol{u}$ based on (2.8) and $|\tilde{\nabla}\tilde{p}'|\ll|\tilde{\nabla}\langle\tilde{p}\rangle|$ as

$$\langle\tilde{u}_i\rangle=-\tilde{k}\left(\frac{\partial\langle\tilde{p}\rangle}{\partial\tilde{x}_i}-(\rho_0/\Delta\rho+\langle C\rangle)\frac{\partial\tilde{z}}{\partial\tilde{x}_i}\right). \tag{2.18}$$

Taking the divergence of this expression and combining it with $\tilde{\nabla}\cdot\langle\tilde{\boldsymbol{u}}\rangle=0$, which results from (2.5), leads to an equation for the mean pressure $\langle\tilde{p}\rangle$. Therefore, if $\langle C\rangle$ is provided, the mean pressure and velocity fields can be calculated. Equation (2.18) together with (2.8) lead to

$$\tilde{u}_i=\langle\tilde{u}_i\rangle+\underbrace{\tilde{k}\frac{\partial\tilde{z}}{\partial\tilde{x}_i}}_{\tilde{\alpha}_i}C'. \tag{2.19}$$

This equation suggests that the velocity fluctuations can be expressed in terms of concentration fluctuations. Using (2.19), one can reformulate (2.12) and (2.15) to obtain

$$\frac{\partial\langle C\rangle}{\partial\tilde{t}}+\frac{\partial\langle\tilde{u}_i\rangle\langle C\rangle}{\partial\tilde{x}_i}+\frac{\partial\tilde{\alpha}_i\langle C'C'\rangle}{\partial\tilde{x}_i}=\frac{1}{Ra}\frac{\partial^2\langle C\rangle}{\partial\tilde{x}_i\partial\tilde{x}_i}\quad\text{and} \tag{2.20}$$

$$\frac{\partial\langle C'C'\rangle}{\partial\tilde{t}}+\frac{\partial\langle\tilde{u}_i\rangle\langle C'C'\rangle}{\partial\tilde{x}_i}+\frac{\partial\tilde{\alpha}_i\langle C'C'C'\rangle}{\partial\tilde{x}_i}=\frac{1}{Ra}\frac{\partial^2\langle C'C'\rangle}{\partial\tilde{x}_i\partial\tilde{x}_i}-\tilde{\chi}+\tilde{\mathscr{P}} \tag{2.21}$$

with the scalar variance production

$$\tilde{\mathscr{P}}=-2\tilde{\alpha}_i\langle C'C'\rangle\frac{\partial\langle C\rangle}{\partial\tilde{x}_i}. \tag{2.22}$$

Note that $\tilde{\mathscr{P}}$ is now closed, since (2.22) depends only on the dependent variables $\langle C\rangle$ and $\langle C'C'\rangle$ and the known vector $\tilde{\boldsymbol{\alpha}}$. The remaining unclosed terms are $\langle C'C'C'\rangle$ and $\tilde{\chi}$ in (2.21), which are addressed below.

Downloaded from https://www.cambridge.org/core. University of Basel Library, on 30 May 2017 at 17:27:58, subject to the Cambridge Core terms of use, available at https://www.cambridge.org/core/terms. https://doi.org/10.1017/jfm.2014.229

3. Length scales and dissipation rate

Here, we investigate the scaling of the dissipation rate, $\tilde{\chi}$, the smallest and largest length scales, and the spectrum of the concentration variance. Practical consequences for numerical simulations are then discussed, and the LMS approach is introduced.

3.1. *One-dimensional averaged equations*

Our scale analysis starts with the ensemble averaged equations. For simplicity, a two-dimensional domain ($\tilde{x}$–$\tilde{z}$-plane) that is $\tilde{L}_x$-periodic in the $\tilde{x}$ direction and extends to $\pm\infty$ in the $\tilde{z}$ direction is considered. For convenience, we take $\tilde{k} = 1$. At time $\tilde{t} = 0$, the concentration $C(\tilde{x}, \tilde{z}, \tilde{t})$ has a sharp interface at a constant $\tilde{z}$, where it changes from zero to unity for decreasing $\tilde{z}$. Since our two-dimensional domain is statistically homogeneous in the horizontal $\tilde{x}$ direction, and if we assume that we sample a sufficiently large number of fingers in that direction, then we can assume spatial ergodicity. These assumptions lead to

$$\langle C(\tilde{z}, \tilde{t})\rangle = \lim_{\tilde{L}_x\to\infty} \frac{1}{\tilde{L}_x} \int_0^{\tilde{L}_x} C(\tilde{x}, \tilde{z}, \tilde{t})\, \mathrm{d}\tilde{x} \tag{3.1}$$

$$\text{and} \quad \langle \tilde{u}_i(\tilde{z}, \tilde{t})\rangle = \lim_{\tilde{L}_x\to\infty} \frac{1}{\tilde{L}_x} \int_0^{\tilde{L}_x} \tilde{u}_i(\tilde{x}, \tilde{z}, \tilde{t})\, \mathrm{d}\tilde{x} = 0 \tag{3.2}$$

for all time. The last equality, i.e. $\langle\tilde{\boldsymbol{u}}\rangle = 0$, results from $\tilde{\boldsymbol{\nabla}} \cdot \langle\tilde{\boldsymbol{u}}\rangle = 0$ and $\langle\tilde{\boldsymbol{u}}\rangle$ being independent of $\tilde{x}$. At later times with high Ra, one obtains the simplified one-dimensional averaged equations

$$\frac{\partial\langle C\rangle}{\partial\tilde{t}} + \frac{\partial\langle C'C'\rangle}{\partial\tilde{z}} = 0 \tag{3.3}$$

$$\text{and} \quad \frac{\partial\langle C'C'\rangle}{\partial\tilde{t}} + \frac{\partial\langle C'C'C'\rangle}{\partial\tilde{z}} = -\tilde{\chi} - 2\langle C'C'\rangle\frac{\partial\langle C\rangle}{\partial\tilde{z}}. \tag{3.4}$$

Closure is required for the triple correlation and $\tilde{\chi}$ in (3.4). Here, we assume that the PDF $f(c)$ can be parameterized in terms of $\langle C\rangle$ and $\langle C'C'\rangle$ independent of Ra. Now, if one can show that $\tilde{\chi}$ is independent of Ra, then the system (3.3)–(3.4) would admit a self-similar solution.

To see this, we consider $\langle C\rangle$ and $\langle C'C'\rangle$ at location z and time t. With the reference length scale H, one obtains the Rayleigh number $Ra = \bar{u}H/D$ and the non-dimensional location $\tilde{z} = z/H$ and time $\tilde{t} = t\bar{u}/H$. For another length scale $H^* = \beta H$ (with $\beta > 0$), one obtains the Rayleigh number $Ra^* = \bar{u}H^*/D = \beta Ra$. From Rayleigh number independence (assuming that both Ra and Ra^* are large), it follows that the same solution is recovered at $\tilde{z} = z/H = z^*/H^*$ and $\tilde{t} = t\bar{u}/H = t^*\bar{u}/H^*$ with either reference length scale H or H^*. Therefore, in z–t space, one obtains $\langle C\rangle(z, t) = \langle C\rangle(z^* = \beta z, t^* = \beta t)$ and $\langle C'C'\rangle(z, t) = \langle C'C'\rangle(z^*, t^*)$, which leads to

$$\langle C\rangle(\tilde{z}, \tilde{t}) = \langle C\rangle(\beta\tilde{z}, \beta\tilde{t}) \tag{3.5}$$

$$\langle C'C'\rangle(\tilde{z}, \tilde{t}) = \langle C'C'\rangle(\beta\tilde{z}, \beta\tilde{t}) \tag{3.6}$$

in the $\tilde{z}$–$\tilde{t}$ space. For $\beta = \tilde{t}^{-1}$ and with the similarity variable $\xi = \tilde{z}/\tilde{t}$, one obtains the similarity relation

$$\langle C\rangle(\tilde{z}, \tilde{t}) = \langle C\rangle(\xi, 1) = \langle C\rangle(\xi), \tag{3.7}$$

$$\langle C'C'\rangle(\tilde{z}, \tilde{t}) = \langle C'C'\rangle(\xi, 1) = \langle C'C'\rangle(\xi). \tag{3.8}$$

Next, we introduce the concept of the variance spectrum. Then, we show that $\tilde{\chi}$ is indeed independent of Ra for high Rayleigh numbers.

Downloaded from https://www.cambridge.org/core. University of Basel Library, on 30 May 2017 at 17:27:58, subject to the Cambridge Core terms of use, available at https://www.cambridge.org/core/terms. https://doi.org/10.1017/jfm.2014.229

3.2. *Variance spectrum*

The starting point is a cascade process for the variance density

$$V_{3D}(\boldsymbol{\kappa}) \quad \text{with } \langle C'C' \rangle = \int_{\mathbb{R}^3} V_{3D}(\boldsymbol{\kappa})\, \mathrm{d}\kappa_1\, \mathrm{d}\kappa_2\, \mathrm{d}\kappa_3 \tag{3.9}$$

in wavenumber space. This expression is similar to that proposed by Richardson (1922) for the spectrum of turbulent energy. Note that $\boldsymbol{\kappa} = (\kappa_1, \kappa_2, \kappa_3)^{\mathrm{T}}$ is the three-dimensional wavenumber vector. However, for the following discussion, the one-dimensional spectrum

$$V(\kappa) \quad \text{with } \langle C'C' \rangle \approx \int_{\mathbb{R}} V(\kappa)\, \mathrm{d}\kappa, \tag{3.10}$$

where $\kappa = |\boldsymbol{\kappa}|$, is employed. The scale $l = 2\pi/\kappa$, which has to be understood in a spectral sense, characterizes variations predominantly in the horizontal direction.

We now assume that scalar variance production occurs mainly at wavenumbers smaller than κ_{coarse}. This assumption is justified below. With that, the average rate $\chi_c(\kappa)$ of nonlinear transfer of V from modes with length scale $l = 2\pi/\kappa$ and characteristic velocity u_l to higher wavenumber modes is caused by the convective term in (2.2). Therefore,

$$\chi_c(\kappa) \sim \frac{u_l}{l}. \tag{3.11}$$

From (2.19), we can see that the fluctuating velocity is proportional to C'; therefore, it scales with $\langle C'C' \rangle^{1/2}$. The characteristic velocity associated with a given wavenumber, κ, is therefore proportional to the square root of V, and in order to have the correct dimensions, it must also be proportional to $\kappa^{1/2}$. Thus, $u_l \sim (V(\kappa)\kappa)^{1/2}\bar{u}$. The diffusion term in (2.2), on the other hand, is responsible for (scalar) variance dissipation, which can be estimated as

$$\chi_d(\kappa) \sim \frac{D}{l^2}. \tag{3.12}$$

The ratio

$$\frac{\chi_d(\kappa)}{\chi_c(\kappa)} \sim \frac{D}{u_l l} = \frac{1}{Ra_l}, \tag{3.13}$$

shows that for large Ra_l, nonlinear convective transfer is dominant compared with diffusive dissipation. We further assume that production of V is negligible at high wavenumbers (confirmed later). Now, since χ_d scales with κ^2 (see (3.12)), then if Ra is large enough, there exists an intermediate wavenumber range, say between κ_{coarse} and κ_{fine}, where both production and dissipation of variance can be neglected. For this intermediate range, we show later that Ra_l scales with κ^{-2}, i.e. that χ_d/χ_c is negligible for small wavenumbers. On the other hand, for large wavenumbers (i.e. $\kappa > \kappa_{fine}$), diffusive dissipation is dominant. Based on this conceptual framework and under the assumption of equilibrium between κ_{coarse} and κ_{fine}, $\chi_c(\kappa)$ must be approximately constant in the intermediate wavenumber range, which is illustrated in figure 1. So, we write

$$\chi_c(\kappa) \approx \chi. \tag{3.14}$$

In the case of such a separation between variance production and dissipation, and if one can assume equilibrium for the fine scale dynamics, i.e. for $\kappa > \kappa_{coarse}$, the variance flux across κ_{coarse} (from left to right in the κ space) must match the flux

Downloaded from https://www.cambridge.org/core. University of Basel Library, on 30 May 2017 at 17:27:58, subject to the Cambridge Core terms of use, available at https://www.cambridge.org/core/terms. https://doi.org/10.1017/jfm.2014.229

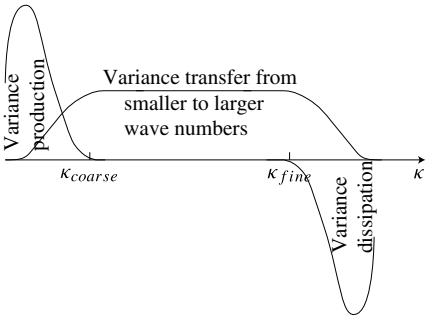

FIGURE 1. Sketch of variance production, dissipation and nonlinear transfer rates as functions of the wavenumber κ.

across κ_{fine} and must be equal to the total dissipation $\chi = \int_{\kappa_{fine}}^{\infty} \chi_d \, \mathrm{d}\kappa$. From this it can be concluded that χ is determined at $\kappa < \kappa_{coarse}$. The length and velocity scales of the large modes at $\kappa = \kappa_{coarse}$ can be estimated as

$$l_{coarse} \sim H \quad \text{and} \quad u_{l_{coarse}} \sim \bar{u} \langle C'C' \rangle^{1/2}, \tag{3.15a,b}$$

and thus one obtains

$$\chi \sim \langle C'C' \rangle^{1/2} \frac{\bar{u}}{H}. \tag{3.16}$$

From (2.17), it follows that $\tilde{\chi} \sim \langle C'C' \rangle^{1/2}$, and thus independent of Ra in agreement with Hidalgo *et al.* (2012).

3.3. *Universal spectrum and similarity hypotheses*

For modes with wavenumbers between κ_{coarse} and κ_{fine}, the length and velocity scales are

$$l \sim \kappa^{-1} \quad \text{and} \quad u_l \sim (V(\kappa)\kappa)^{1/2} \bar{u}, \tag{3.17a,b}$$

and from

$$\chi(\kappa) \sim \frac{u_l}{l} \tag{3.18}$$

one obtains

$$V(\kappa) \sim \chi^2 \bar{u}^{-2} \kappa^{-3} \sim \frac{\langle C'C' \rangle}{H^2} \kappa^{-3} \tag{3.19}$$

for the scaling of the variance spectrum. Owing to the κ^{-3} dependence, most of the scalar variance is contained in the large-scale modes. Since the variance production, $\tilde{\mathscr{P}}$, is directly proportional to the variance, one can conclude that V is produced at a rate proportional to κ^{-3}, which supports the assumption made earlier that the scalar variance production occurs mainly in the small-wavenumbers part of the spectrum.

Now, based on the above discussion, we postulate the following two hypotheses similar to those by Kolmogorov (1941) proposed in the context of turbulent flows for the velocity spectrum (see appendix A).

First similarity hypothesis for miscible gravity fingering. In homogeneous porous media at sufficiently high Rayleigh numbers Ra, there exists a wavenumber, κ_{coarse}, beyond which the statistics of the modes depend only on χ and D.

Downloaded from https://www.cambridge.org/core. University of Basel Library, on 30 May 2017 at 17:27:58, subject to the Cambridge Core terms of use, available at https://www.cambridge.org/core/terms. https://doi.org/10.1017/jfm.2014.229

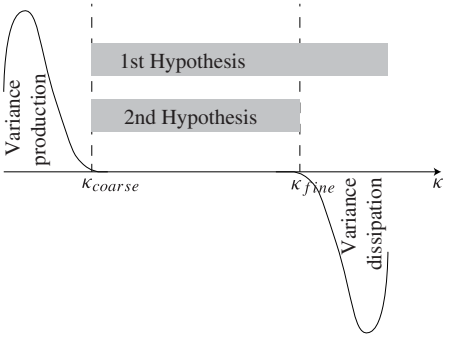

FIGURE 2. Sketch of validity range for the two similarity hypotheses.

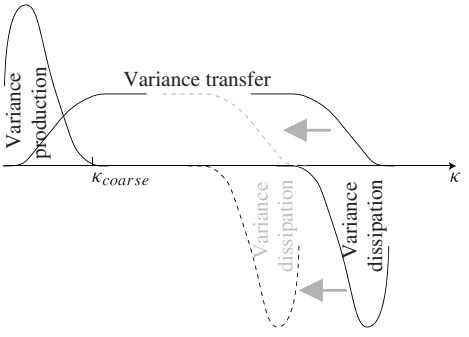

FIGURE 3. Illustration of dependence on D. The dashed lines indicate the shift of diffusive dissipation towards lower wavenumbers, if D is increased, and that χ_c in the intermediate range essentially remains unaffected.

Second similarity hypothesis for miscible gravity fingering. In homogeneous porous media at sufficiently high Rayleigh numbers Ra, there exists a wavenumber range between κ_{coarse} and κ_{fine}, for which the statistics of the modes depend only on χ.

The applicability range for the two hypotheses is depicted in figure 2. From the first similarity hypothesis, it follows that l_{fine} is a function of χ and D, and simple dimensional analysis leads to

$$l_{fine} \sim \left(\frac{D}{\chi}\right)^{1/2} = \left(\frac{HD}{\bar{u}\langle C'C'\rangle^{1/2}}\right)^{1/2}. \tag{3.20}$$

For the ratio of the smallest to the largest length scales, one obtains

$$\frac{l_{fine}}{l_{coarse}} \sim \left(\frac{\bar{u}H}{D}\right)^{-1/2} \langle C'C'\rangle^{-1/4} = Ra^{-1/2}\langle C'C'\rangle^{-1/4}. \tag{3.21}$$

Note that as long as the κ_{fine} modes do not interfere with the κ_{coarse} ones, then changing Ra (e.g. by increasing D) changes the ratio l_{fine}/l_{coarse}, but it does not affect the large-scale behaviour. This is illustrated by the sketch in figure 3.

In the following section we provide confirmation for the theoretical scale analysis regarding the variance spectrum. First, it is shown that for large enough Rayleigh

Downloaded from https://www.cambridge.org/core. University of Basel Library, on 30 May 2017 at 17:27:58, subject to the Cambridge Core terms of use, available at https://www.cambridge.org/core/terms. https://doi.org/10.1017/jfm.2014.229

numbers, the mean concentration profiles obtained for the set-up introduced in § 3.1 are self-similar. From that one can conclude that χ is independent of Ra, which confirms that the production and dissipation spectra are separated in wavenumber space. Note that the latter property was the main assumption in the spectral analysis. Further, it is shown that the scaling of the finger width is as predicted by the analysis.

More explanations regarding Kolmogorov's similarity hypotheses for turbulent flows and the analogy between the spectral analysis presented above and the turbulence energy spectrum are provided in appendix A.

3.4. *Practical consequences for numerical simulation*

Our findings have the important consequence that one can consider the same scenario, but for a lower Ra than the actual one, such that all of the relevant modes can be resolved adequately on a coarser computational mesh. Therefore, we suggest replacing (2.1) and (2.2) with

$$\frac{\partial}{\partial x_i}\overbrace{\left(\frac{k}{\mu\phi}\left(\frac{\partial \hat{p}}{\partial x_i}-\rho(\hat{C})g\frac{\partial z}{\partial x_i}\right)\right)}^{-\hat{u}_i}=0 \tag{3.22}$$

$$\frac{\partial \hat{C}}{\partial t}+\frac{\partial \hat{u}_i\hat{C}}{\partial x_i}=\frac{\partial}{\partial x_i}\left(D_e^{LMS}\frac{\partial \hat{C}}{\partial x_i}\right), \tag{3.23}$$

where $\hat{C}$ can be interpreted as the spatially coarsened scalar field considering a 'resolution' length-scale Δ, and where D_e^{LMS} is the effective diffusion coefficient. This approach, which we refer to as LMS, involves performing a numerical simulation at a different (lower) Rayleigh number, which can be done using coarse grids that resolve Δ. The modification is similar to the subgrid-scale modelling approach by Smagorinsky (1963) for large eddy simulation (LES) of turbulent flows. Here, we suggest modifying Ra by choosing the effective diffusion coefficient as

$$D_e^{LMS}=\max(D,\,(c^{LMS}\Delta)^2\bar{u}|\nabla\hat{C}|), \tag{3.24}$$

where c^{LMS} is a model constant. Note that (3.24) is a closure model. It is motivated by a similar model, i.e. (B 1), which is often used in LES (Smagorinsky model) to capture the effective viscosity (residual plus fluid viscosity). The model constant c^{LMS} has to be chosen such that $D_e^{LMS}=D$, where the resolution length scale Δ (proportional to the grid spacing) is sufficiently small to resolve the diffusive flux. On the other hand, a properly chosen model constant also ensures that the concentration gradients remain limited by using $D_e^{LMS}=(c^{LMS}\Delta)^2\bar{u}|\nabla\hat{C}|>D$ wherever necessary. In other words, with an ideal choice of c^{LMS}, as much as possible of the fine-scale concentration variations are captured by increasing the diffusion coefficient from D to D_e^{LMS}. The choice of c^{LMS} ensures that the discretization of the diffusive term is accurate everywhere. Therefore, its optimal value depends on both the scheme and the grid (stretched, structured, unstructured, etc.). Since the effective local Rayleigh number scales with $1/D_e^{LMS}$ and thus is smaller for coarse grids, the required grid resolution is directly linked to the question of the minimal Rayleigh number beyond which the coarse-scale dynamics become independent of Ra. This is investigated to some extent in § 4.1, but more systematic studies are required to quantify the minimal grid resolution in combination with the proposed model.

The similarity of LMS with LES for turbulent flows is described in appendix B.

Downloaded from https://www.cambridge.org/core. University of Basel Library, on 30 May 2017 at 17:27:58, subject to the Cambridge Core terms of use, available at https://www.cambridge.org/core/terms. https://doi.org/10.1017/jfm.2014.229

Ra	L_x	L_z	Grid $(x \times z)$
2 000	$4H$	H	1600×400
5 000	$2H$	H	1600×800
10 000	H	H	1600×1600
20 000	H	H	1600×1600
40 000	H	$2H$	1600×3200
80 000	H	H	3200×3200

TABLE 1. Domain sizes and grid resolutions for different simulations of the case depicted in figure 4.

4. Numerical investigation

In this section, results that support the scale analysis are provided. It is shown that (i) χ is independent of Ra, if the Rayleigh number is large enough, (ii) the scaling of the finger width with Ra and time is consistent with the analysis, (iii) the smallest length scales grow with $Ra^{-1/2}$ and (iv) evidence is provided that the coarse-scale fingering behaviour becomes essentially independent of Ra. Moreover, for the one-dimensional test case of § 3.1, simple closure of the ensemble averaged equations is proposed and validated using DNS.

4.1. *DNS and LMS*

Unlike in § 3.1, where a vertically infinite domain was considered, we employ a finite domain to enable a computational analysis and verification of the proposed theory. Equations (2.1) and (2.2) are solved for different Rayleigh numbers on a domain with extensions L_x and L_z in the x and z directions, respectively, as listed in table 1. At the top and bottom of the domain, we have no flow. Periodic boundary conditions are applied on the sides. For the finite-volume computations, Cartesian grids with resolutions listed in table 1 are employed. A sketch of the test case is shown in figure 4. For the most challenging case with $Ra = 80\,000$, the selected discretization parameters lead to a resolution with 11 and 44 grid cells on average per finger at the beginning ($\tilde{t} = 0.1$) and the end of the simulation ($\tilde{t} = 1.5$), respectively. Moreover, coarsening the grid resolution by half, i.e. 1600×1600 cells for $Ra = 80\,000$, does not change the reported statistical quantities significantly.

Note that these studies focus on the long-term fingering behaviour and not on the onset period. Therefore, the details of the initial perturbations are of little importance; here random concentration values (between zero and one) are assigned in a thin band around the initial discontinuity. Figure 5 shows simulation results at $\tilde{t} \in \{0.25, 0.5, 0.75, 1.25\}$ for $Ra = 80\,000$ (a) and $Ra = 20\,000$ (b). One can observe that the long-term nonlinear behaviours are quite similar between the two simulations. This is consistent with observations by previous investigators that the nonlinear flux becomes constant with time and independent of Ra (see Hesse *et al.* 2006; Pau *et al.* 2010). For example, the results in figure 5 demonstrate that the mean behaviour does not change, if Ra is reduced in an LMS from 80 000 to 20 000. This enables a reduction of the computational burden, since a coarser grid can be used. Here, in figure 6, we provide more quantitative evidence for the flux at three different times $\tilde{t} \in \{0.25, 0.75, 1.25\}$. Figure 6($a$) shows $\langle C \rangle$ and figure 6(b) shows $\langle C'C' \rangle$, both as functions of $\tilde{z}$ and $\tilde{t}$ for $Ra = 20\,000$, 30 000 and 80 000. Note that $\langle C'C' \rangle$ is in fact the 'flux' in the mean concentration transport equation (3.3).

Downloaded from https://www.cambridge.org/core. University of Basel Library, on 30 May 2017 at 17:27:58, subject to the Cambridge Core terms of use, available at https://www.cambridge.org/core/terms. https://doi.org/10.1017/jfm.2014.229

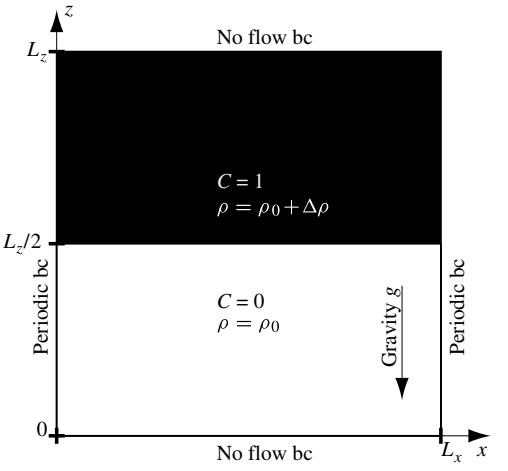

FIGURE 4. Sketch of the statistically one-dimensional test case with initial conditions.

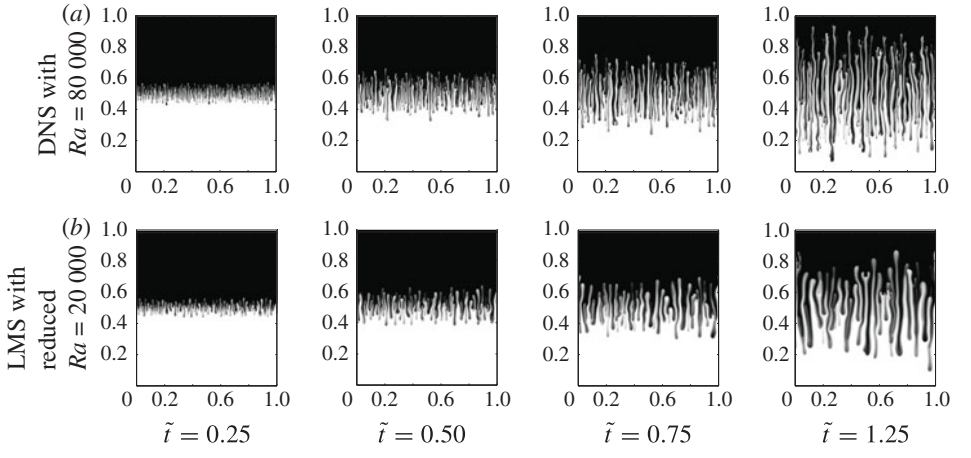

FIGURE 5. Time evolution of gravity fingers for two different Rayleigh numbers.

For the scale analysis, we made the assumption that the dissipative and variance containing subranges are separated, but the analysis does not provide an indication of the *Ra* threshold beyond which this is indeed the case. However, the analysis predicts that the separation becomes more distinct as *Ra* increases. To demonstrate the limit, i.e. to get an idea beyond which *Ra* value the similarity (conclusion from the analysis) holds, results for $Ra = 2000$, 5000, 10 000, 20 000 and 80 000 are shown in figure 7. For Rayleigh numbers up to 10 000, both the mean and variance show considerable differences. However, above $Ra = 20\,000$ and after the initial onset period, the differences become small as shown in figure 6.

These observations also confirm the conclusions drawn in § 3. For example, if the Rayleigh number of the target problem is 80 000, then it is justified to compute the long-term coarse-scale behaviour with an 'artificially' reduced Rayleigh number (e.g. with $Ra = 20\,000$). Thus, coarse grids can be used, which is very promising for field-scale studies where it is not feasible to honour the true (extremely large)

Downloaded from https://www.cambridge.org/core. University of Basel Library, on 30 May 2017 at 17:27:58, subject to the Cambridge Core terms of use, available at https://www.cambridge.org/core/terms. https://doi.org/10.1017/jfm.2014.229

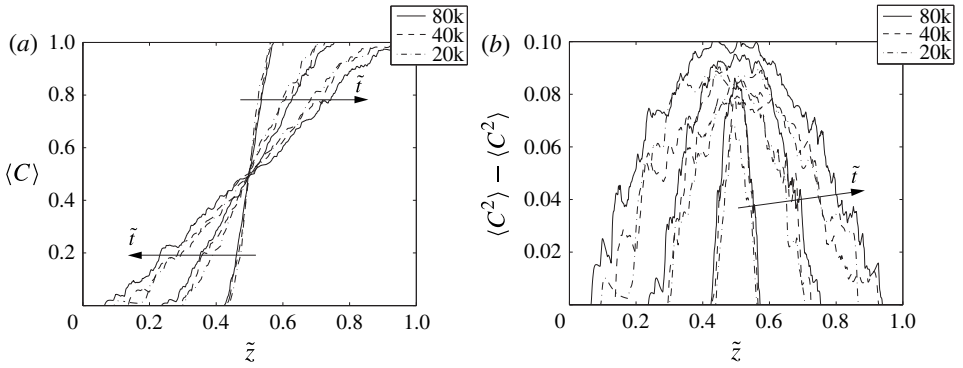

FIGURE 6. One-dimensional averages of DNS results with different Ra: time evolution of the two first moments extracted from DNS data at $\tilde{t} \in \{0.25, 0.75, 1.25\}$.

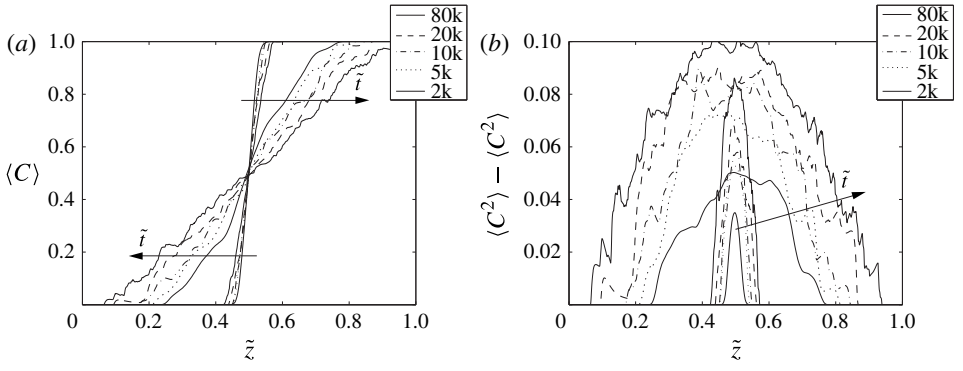

FIGURE 7. One-dimensional averages of DNS results with different Ra: time evolution of the two first moments extracted from DNS data at $\tilde{t} \in \{0.25, 1.25\}$.

Rayleigh number. Note, however, that differences occur during the onset period and that the $Ra = 20\,000$ results are more coarse-grained than those obtained with $Ra = 80\,000$. The symbols in figure 8 show the evolution of the fine-scale finger width at $\tilde{z} = 0.5$ for $Ra = 20\,000$ and $Ra = 80\,000$ extracted from DNS data (estimated as $L_x/n_{C0.5}$, where $n_{C0.5}$ is the number of intersections of $C(x, z = L_z/2)$ with the concentration level 0.5). From (3.21) it follows that $\tilde{l}_{fine}(\tilde{z} = 0.5) \sim Ra^{-1/2}$. Owing to self-similarity $\tilde{l}_{fine}(\tilde{z} = 0.5) \sim \tilde{t}^{1/2}$, which is confirmed by the lines in figure 8 representing

$$\tilde{l}_{fine}(\tilde{z} = 0.5) = \frac{l_{fine}(\tilde{z} = 0.5)}{H} = KRa^{-1/2}\tilde{t}^{1/2} \tag{4.1}$$

with a constant K. Note that (4.1), which is confirmed by empirical data, reflects that the fingers coarsen by diffusion. Thus, it is not surprising that l_{fine} scales with the square roots of both D and t.

4.2. *Closure of one-dimensional ensemble-averaged equations and verification*

Next, closure for the statistically one-dimensional case of (3.3) and (3.4) is proposed and verified using DNS. As shown in § 3.2, $\tilde{\chi}$ is independent of Ra for large Rayleigh

Downloaded from https://www.cambridge.org/core. University of Basel Library, on 30 May 2017 at 17:27:58, subject to the Cambridge Core terms of use, available at https://www.cambridge.org/core/terms. https://doi.org/10.1017/jfm.2014.229

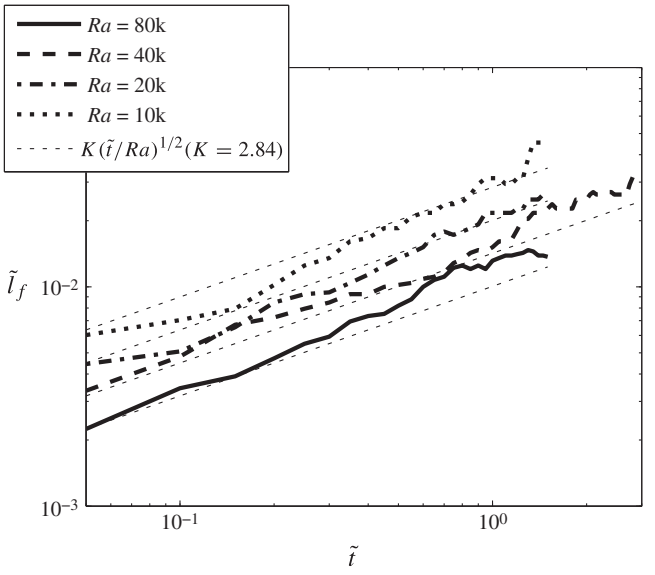

FIGURE 8. Temporal evolution of the fine-scale finger width extracted from DNS data (thick lines) at $\tilde{z} = 0.5$ for different Rayleigh numbers. Also shown are the lines $\tilde{l}_{fine}(\tilde{z} = 0.5) = KRa^{-1/2}\tilde{t}^{1/2}$ with $K = 2.84$.

numbers. So, if we assume that the PDF, $f(c)$, is determined by $\langle C\rangle$ and $\langle C'C'\rangle$, equations (3.3) and (3.4) admit a self-similar solution, i.e. that $\langle C\rangle$ and $\langle C'C'\rangle$ are functions of $\xi = \tilde{z}/\tilde{t}$ only. Further, since $\langle C\rangle(\xi)$ is monotone (see figure 6), the variance becomes a function of the mean. Note that with $\tilde{\chi} = 0$, one would obtain the relation $\langle C'C'\rangle = \langle C\rangle(1 - \langle C\rangle)$. Therefore, we now make the ansatz

$$\langle C'C'\rangle = a\langle C\rangle(1 - \langle C\rangle) \tag{4.2}$$

with $0 < a < 1$. After substitution into (3.3), one obtains the hyperbolic equation

$$\frac{\partial\langle C\rangle}{\partial\tilde{t}} + a\frac{\partial(\langle C\rangle - \langle C\rangle^2)}{\partial\tilde{z}} = 0 \tag{4.3}$$

for $\langle C\rangle$. The wave speed is

$$\lambda = a\frac{\mathrm{d}(\langle C\rangle - \langle C\rangle^2)}{\mathrm{d}\langle C\rangle} = a(1 - 2\langle C\rangle). \tag{4.4}$$

Comparing the minimal and maximal values $\lambda_{min} = -a$ and $\lambda_{max} = a$ for $\langle C\rangle = 1$ and $\langle C\rangle = 0$, respectively, with the DNS results for the case with $Ra = 80\,000$ (figure 6), one obtains $a \approx 0.32$. Figure 9(*a*) shows $\langle C'C'\rangle(\langle C\rangle)$ at $\tilde{t} = 0.1$, 1 and 3.5, which indicates that after some time, a reaches its terminal value. This can be observed more clearly in figure 9(*b*). Finally, figure 10 shows $\langle C\rangle(\tilde{z}, \tilde{t})$ from DNS with $Ra = 80\,000$ and (4.3), and the agreement is quite good.

Note that the employed closure of the ensemble-averaged equations is not necessarily valid for the general case. A discussion of less case-specific closures is presented in appendix C, where the ensemble-averaged Darcy modelling (EADM) approach is introduced.

Downloaded from https://www.cambridge.org/core. University of Basel Library, on 30 May 2017 at 17:27:58, subject to the Cambridge Core terms of use, available at https://www.cambridge.org/core/terms. https://doi.org/10.1017/jfm.2014.229

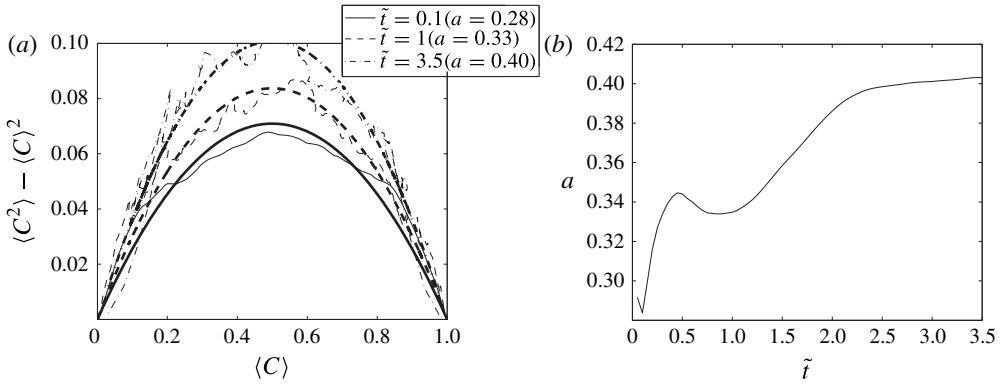

FIGURE 9. In (*a*), $\langle C'C' \rangle (\langle C \rangle)$ at times $\tilde{t} = 0.1$, 1 and 3.5 resulting from the DNS with $Ra = 40\,000$ (thin lines) are compared with closure (4.2) with given values of a (thick lines). In (*b*), $a(\tilde{t})$ resulting from a least-squares fit of closure (4.2) to the DNS is provided.

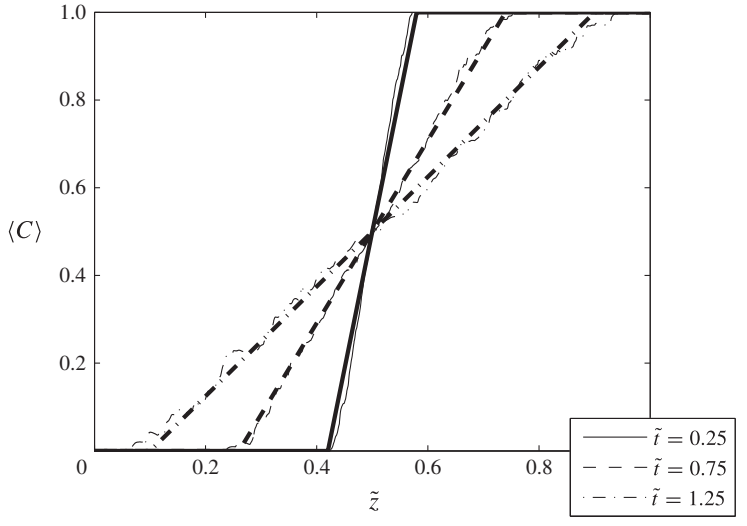

FIGURE 10. Comparison of $\langle C \rangle (\tilde{z}, \tilde{t})$ at times $\tilde{t} = 0.25$, 0.75 and 1.25 resulting from the DNS $Ra = 80\,000$ (thin lines) and analytically based on (4.3) with $a = 0.32$ (thick lines).

4.3. CO_2 *sequestration*

Note that the test case discussed above is only partly representative for CO_2 sequestration scenarios. There it is typical to find the lighter CO_2 phase on top of the immiscible brine. As CO_2 dissolves into the underlying brine, a thin boundary layer forms at the interface, which eventually becomes unstable since the brine density increases with CO_2 concentration. To investigate the dynamics of the resulting miscible gravity fingers (Hewitt *et al.* 2013; Slim *et al.* 2013), an additional test case is analysed here.

The same domain as before is employed with no-flow conditions at the top and bottom and periodic boundary conditions on the sides. This time, however, the initial interface is located at the top, i.e. at $z = L_z$ (see figure 4), with the concentration at the

Downloaded from https://www.cambridge.org/core. University of Basel Library, on 30 May 2017 at 17:27:58, subject to the Cambridge Core terms of use, available at https://www.cambridge.org/core/terms. https://doi.org/10.1017/jfm.2014.229

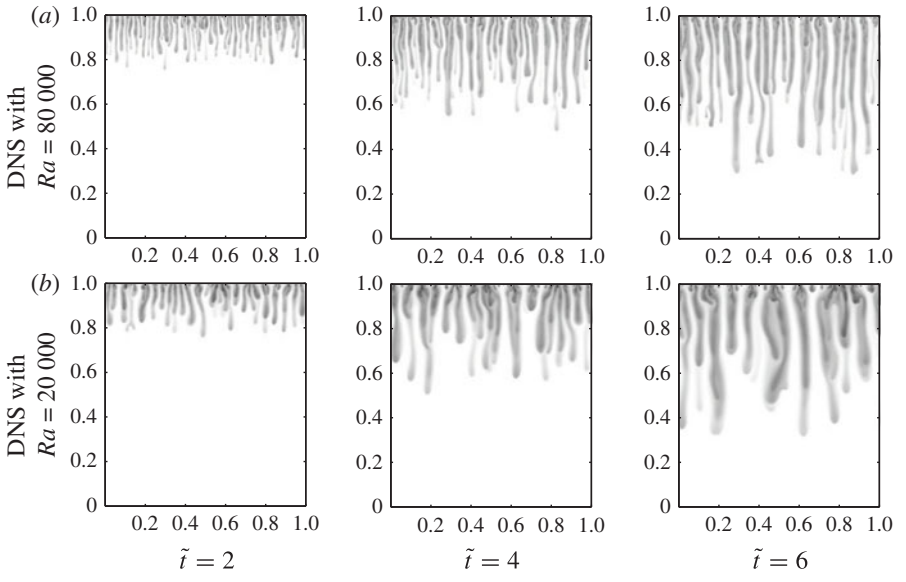

FIGURE 11. Time evolution of gravity fingers for two different Rayleigh numbers.

top boundary equal to one. For the simulations, computational domains of size $L_x = L_z = H$ with resolutions 1600×1600 were applied for all Rayleigh numbers except for $Ra = 80\,000$, where 3200×3200 grid cells were used.

The results with Rayleigh numbers 20 000 and 80 000 are shown in figure 11. In comparison with the case depicted in figure 4, the fingers propagate more slowly, which is caused by the no-flow boundary condition at the top of the domain. For the Rayleigh numbers in figure 11, the finger propagation depth appears to be independent of Ra, which is similar to the previous case. This is further confirmed by the concentration means and variances depicted in figure 12. As in figure 6, there is good agreement between the one-dimensional averages for $Ra = 20\,000$, 40 000 and 80 000. By plotting $\langle C'C' \rangle$ as a function of $\langle C \rangle$ (figure 13), it can be shown that the closure model (4.2) works reasonably well for the present case, but with an adjusted coefficient a.

5. Summary and conclusions

We have developed a conceptual and mathematical framework for scale analysis of unstable miscible convection in porous media, which is important for subsurface CO_2 sequestration in deep saline aquifers. It is widely recognized that the evolution dynamics of density-driven convection in natural porous media are highly nonlinear, and that the physical interactions involve wide ranges of length and time scales. For simple settings (e.g. two-dimensional, homogeneous domains), one can calculate the long-term behaviours of the unstable CO_2-saturated brine plumes using DNS, which resolve the full range of scales. In practice, however, the target subsurface geological formation is usually heterogeneous with complex structural geometry and boundary conditions. Moreover, miscible convection may be just one of many transport mechanisms that govern the distribution of fluids in the large-scale subsurface sequestration formation of interest. Thus, it is not feasible to employ DNS to make long-term predictions of unstable flows in practical settings, and there is a need to

Downloaded from https://www.cambridge.org/core. University of Basel Library, on 30 May 2017 at 17:27:58, subject to the Cambridge Core terms of use, available at https://www.cambridge.org/core/terms. https://doi.org/10.1017/jfm.2014.229

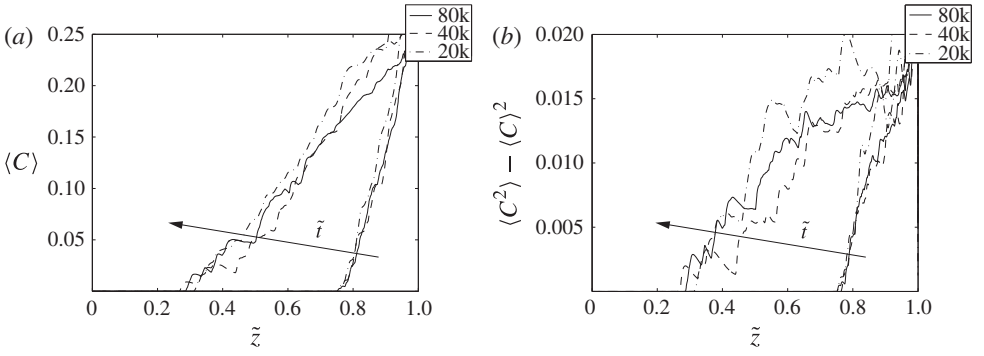

FIGURE 12. One-dimensional averages of DNS results with different Ra and concentration interface at the top of the domain: time evolution of the two first moments extracted from DNS data at $\tilde{t} \in \{2, 6\}$.

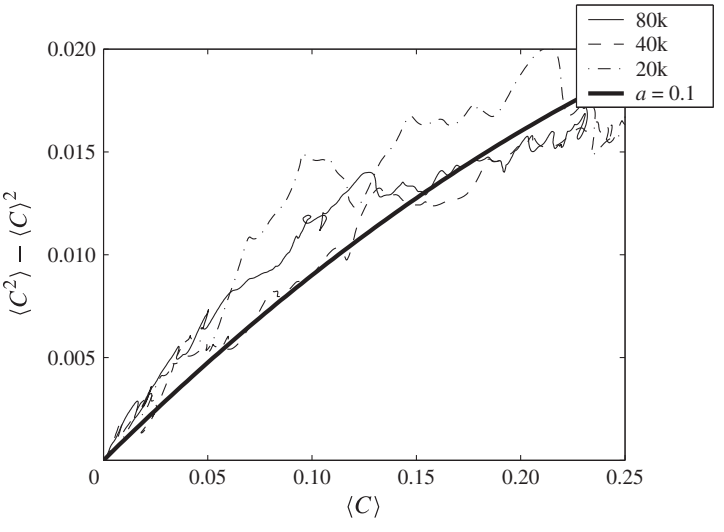

FIGURE 13. Plot of $\langle C'C' \rangle (\langle C \rangle)$ at time $\tilde{t} = 6$ resulting from DNS with different Ra (thin lines) are compared with closure (4.2) with $a = 0.1$ (thick line).

develop accurate solution methods that are based on coarse-scale descriptions of the flow physics.

The key component of our scale analysis relates to the conservation equation of the concentration variance. The so-called transverse flow equilibrium assumption (see Yortsos 1995) is employed to relate velocity and concentration deviations. This simplifies the problem by decoupling the flow (pressure and velocity) from the transport (concentration). While the variance production term is closed, the variance balance equation has two unclosed terms that require modelling. The first term contains the third concentration moment, which contributes to the nonlinear flux (transport). The second is a source term that represents the variance dissipation rate. To deal with the triple correlation term, we assume for vertical, statistically one-dimensional gravity fingering that the concentration PDF can be parameterized in terms of the concentration mean and variance. The dissipation rate is then estimated

Downloaded from https://www.cambridge.org/core. University of Basel Library, on 30 May 2017 at 17:27:58, subject to the Cambridge Core terms of use, available at https://www.cambridge.org/core/terms. https://doi.org/10.1017/jfm.2014.229

based on our scale analysis. The conceptual framework, which is supported by analysis and DNS results, is based on the idea that the contribution of small-scale structures (fingers) to the total production of the concentration variance is quite small, and that the large-scale features are responsible for the bulk of the concentration variance production. Even though the dynamics are quite complex, the nonlinear evolution regime (where linear stability analysis is not valid) gets established after a relatively short onset period. As a result, the long-term evolution of the unstable plumes is amenable to representations using length (and time) scales that are much larger than the small diffusive scales associated with the early onset period. This does not mean that the small-scale dynamics are not important; instead, the idea is to account for the impact of nonuniform flow at small scales on the long-term dynamics using simple, yet accurate, subscale models.

An important conclusion of the scale analysis is that the governing equations can be solved using length and time scales that are coarse compared with the scales dictating the instability behaviours during the relatively short onset period. In fact, for sufficiently high Rayleigh numbers, the statistical behaviours can be described accurately, if Ra is reduced to a level that allows for simulation on a grid, which would be too coarse for the actual Rayleigh number. This is the main justification for the LMS approach introduced in this paper. LMS is based on resolving the low-wavenumber dynamics only, whereas the effect of the unresolved scales on the large ones is captured by a modified effective Rayleigh number. Further justification for LMS is provided by DNS computations, which were used to analyse the rates of production and dissipation of the ensemble concentration variance. Overall, we find that the nonlinear CO_2 flux is nearly constant with time and is also independent of Ra. These findings are consistent with previous investigations. The DNS data clearly indicate that the dissipation rate is dominated by the low-wavenumber modes and does not vary with Ra (beyond a certain lower value). Scale analysis shows that the variance production associated with the unstable modes is proportional to κ^{-3}, so that the relative contribution to the concentration variance from the large-wavenumber end of the spectrum is small; this analysis is supported by the DNS results. While a simple setting is used to demonstrate the methodology, we believe that the concepts presented here are applicable to the wider class of unstable flows in natural porous media.

We plan to investigate the applicability of LMS to miscible convection in large-scale heterogeneous formations. Other areas where LMS may be useful include modelling unstable miscible flow with reactions. Extending LMS to immiscible flows in the presence of strong capillarity and buoyancy effects, which are quite relevant to the (up-dip) migration of subsurface CO_2 plumes, is a longer-term target. Further, the proposed closures for EADM (see appendix C) will be investigated.

Acknowledgements

The authors thank Cédric de Crousaz and Antonia Baumann for their help during the preparation of this manuscript. Support by the PI of Abu Dhabi is also acknowledged.

Appendix A

The first and second similarity hypotheses for miscible gravity fingering presented in § 3.3 are inspired by the first and second similarity hypotheses for turbulent flows by Kolmogorov (1941, 1962).

Downloaded from https://www.cambridge.org/core. University of Basel Library, on 30 May 2017 at 17:27:58, subject to the Cambridge Core terms of use, available at https://www.cambridge.org/core/terms. https://doi.org/10.1017/jfm.2014.229

Kolmogorov's first similarity hypothesis. In turbulent flows at sufficiently high Reynolds number, there exists a wavenumber κ_{coarse}, beyond which the statistics of the velocity modes depend only on the turbulence dissipation rate and the kinematic velocity.

Kolmogorov's second similarity hypothesis. In turbulent flows at sufficiently high Reynolds number, there exists a wavenumber range between κ_{coarse} and κ_{fine}, for which the statistics of the velocity modes depend only on the turbulence dissipation rate.

From these hypotheses, one can conclude that:

(i) most of the turbulent kinetic energy is stored in the low-wavenumber modes;
(ii) turbulent kinetic energy production occurs at low wavenumbers;
(iii) most of the energy dissipation takes place at the largest wavenumbers;
(iv) the turbulent kinetic energy is transferred from lower to larger wavenumber modes until the largest wavenumbers are reached; and
(v) that the mean flow and the statistics of the low-wavenumber modes are essentially independent of the Reynolds number.

Note that similar conclusions were reached here for unstable gravity fingering in miscible porous media flow if one replaces 'turbulent kinetic energy' with 'scalar variance', 'energy dissipation' with 'scalar variance dissipation' and 'Reynolds number' with 'Rayleigh number'.

Appendix B

The LMS approach discussed in § 4.1 is quite similar to LES for turbulent flows (Pope 2000, chapter 13), where only the large energy-containing eddies (note that here energy refers to turbulent kinetic energy, which is proportional to the velocity variance) are resolved (represented by the spatially filtered velocity field). The effect of the small unresolved eddies on the larger ones is accounted for by a residual scale model, many of which are based on a simple eddy viscosity ansatz. The widely used Smagorinsky model (see Smagorinsky 1963), for example, treats the collective effects of the unresolved residual scales on the resolved ones by replacing the kinematic viscosity ν with

$$\nu_e = \nu + (c_s \Delta)^2 |\hat{S}|, \tag{B 1}$$

where c_s is the Smagorinsky constant, Δ the filter width, and $|\hat{S}|$ the magnitude of the filtered rate-of-strain tensor

$$\hat{S}_{ij} = \frac{1}{2}\left(\frac{\partial \hat{U}_j}{\partial x_i} + \frac{\partial \hat{U}_i}{\partial x_j}\right). \tag{B 2}$$

Note that the latter is proportional to gradients of the filtered velocity $\hat{\boldsymbol{U}}$, and that (B 1) is similar to closure (3.24). With (B 1), the modelled filtered momentum equation attains the same form as the unfiltered Navier–Stokes equation, except that the viscosity is replaced by ν_e, i.e. the effective viscosity is 'adequately' increased compared with ν in order to account for residual scale effects. At least for high-Reynolds-number free-shear flows, all of this is well motivated by Kolmogov's two similarity hypotheses (see Kolmogorov 1941, 1962) and by the turbulent kinetic energy spectrum.

Downloaded from https://www.cambridge.org/core. University of Basel Library, on 30 May 2017 at 17:27:58, subject to the Cambridge Core terms of use, available at https://www.cambridge.org/core/terms. https://doi.org/10.1017/jfm.2014.229

Appendix C

Here, closures of the ensemble-averaged equations

$$\frac{\partial}{\partial x_i}\overbrace{\left(\frac{k}{\mu\phi}\left(\frac{\partial\langle p\rangle}{\partial x_i}-\rho(\langle C\rangle)g\frac{\partial z}{\partial x_i}\right)\right)}^{-\langle u_i\rangle}=0 \tag{C 1}$$

$$\frac{\partial\langle C\rangle}{\partial t}+\frac{\partial\langle u_i\rangle\langle C\rangle}{\partial x_i}+\frac{\partial}{\partial x_i}\left(\frac{kg\Delta\rho}{\mu\phi}\frac{\partial z}{\partial x_i}\langle C'C'\rangle\right)=\frac{\partial}{\partial x_i}\left(D\frac{\partial\langle C\rangle}{\partial x_i}\right) \tag{C 2}$$

are considered, together with the variance equation

$$\frac{\partial\langle C'C'\rangle}{\partial t}+\frac{\partial\langle u_i\rangle\langle C'C'\rangle}{\partial x_i}+\frac{\partial\alpha_i\langle C'C'C'\rangle}{\partial x_i}=D\frac{\partial^2\langle C'C'\rangle}{\partial x_i\partial x_i}-\chi+\mathscr{P} \tag{C 3}$$

and $\alpha_i=\mu^{-1}\phi^{-1}kg\Delta\rho(\partial z/\partial x_i)$. Hereafter, we refer to this approach as EADM. While $\mathscr{P}$ appears in closed form, modelling is required for χ and the third concentration moment. One possibility to model the triple correlation is to employ a gradient diffusion assumption, i.e.

$$-\alpha_i\langle C'C'C'\rangle\approx\underbrace{\left(c^{EAD}\frac{\partial z}{\partial x_i}\frac{\alpha_j^2}{\chi}\right)}_{D_{ij}^{EAD}}\frac{\partial\langle C'C'\rangle}{\partial x_j}, \tag{C 4}$$

where c^{EAD} is a model constant. For χ, on the other hand, a general closure approach is more difficult to obtain. One possibility is to solve an extra transport equation for χ, e.g. of the form

$$\frac{\partial\chi}{\partial t}+\frac{\partial\langle u_i\rangle\chi}{\partial x_i}=\frac{\partial}{\partial x_i}\left(\frac{D_{ij}^{EAD}}{\sigma^{EAD}}\frac{\partial\chi}{\partial x_j}\right)+c_{\chi_1}^{EAD}\frac{\mathscr{P}\chi}{\langle C'C'\rangle}-c_{\chi_2}^{EAD}\frac{\chi^2}{\langle C'C'\rangle}, \tag{C 5}$$

where σ^{EAD}, $c_{\chi_1}^{EAD}$ and $c_{\chi_2}^{EAD}$ are further model constants; but this approach has not been investigated so far and is not pursued further in this paper. Instead, in § 4.2 an algebraic closure for the concentration variance is proposed for the special case described in § 3.1. Note, however, that (C 5) resembles the modelled turbulence dissipation rate transport equation often used for Reynolds-averaged Navier–Stokes (RANS) modelling of turbulent flows (Pope 2000, equation (10.53)), and that the gradient diffusion ansatz (C 4) is motivated by equation (11.147) in Pope (2000). The similarity between EADM and RANS modelling is discussed in the following paragraph.

In RANS modelling of turbulent flows, the velocity covariance tensor (Reynolds stress tensor) has to be modelled, like the scalar variance for EADM. Different closure strategies have been proposed; here only one is mentioned, i.e. the Reynolds stress modelling approach, which is based on solving six additional equations for each Reynolds stress. To achieve closure, a turbulent transport term (involving velocity triple correlations and covariance of pressure and velocity) and the turbulence dissipation rate have to be modelled. The former is typically described by a gradient diffusion ansatz, i.e. it is set proportional to the Reynolds stress gradients. The

Downloaded from https://www.cambridge.org/core. University of Basel Library, on 30 May 2017 at 17:27:58, subject to the Cambridge Core terms of use, available at https://www.cambridge.org/core/terms. https://doi.org/10.1017/jfm.2014.229

corresponding tensorial diffusion coefficient, according to dimensional and scale analysis, is a function of the Reynolds stress tensor and the turbulence dissipation rate, for which another modelled transport equation is solved. Note the similarity between such RANS models for turbulent flows and the proposed EADM approach for miscible gravity fingering. Like the Reynolds stresses in the Reynolds stress closure described above, the scalar flux in (C 2) can be closed by solving the scalar variance equation (C 3). Further, in a manner similar to the turbulent transport term in the Reynolds stress transport equations, the gradient diffusion ansatz (C 4) may be adapted to close the triple correlation term in EADM. Then, one can obtain χ by solving the scalar dissipation rate transport equation (C 5).

REFERENCES

BACHU, S., GUNTHER, W. D. & PERKINS, E. H. 1994 Aquifer disposal of CO_2: hydrodynamic and mineral trapping. *Energy Convers. Manage.* **35**, 269–279.

ENNIS-KING, J. & PATERSON, L. 2005 Role of convective mixing in the long-term storage of carbon dioxide in deep saline formations. *SPE J.* **3**, 349–356.

ENNIS-KING, J., PRESTON, I. & PATERSON, L. 2005 Onset of convection in anisotropic porous media subject to a rapid change in boundary conditions. *Phys. Fluids* **17**, 084107.

FARAJZADEH, R., SALIMI, H., ZITHA, P. & BRUINING, H. 2007 Numerical simulation of density-driven natural convection in porous media with application for CO_2 injection projects. *Intl J. Heat Mass Transfer* **50**, 5054–5064.

GASDA, S. E., NORDBOTTEN, J. M. & CELIA, M. A. 2011 Vertically averaged approaches for CO_2 migration with solubility trapping. *Water Resour. Res.* **47**, W05528.

GHESMAT, K., HASSANZADEH, H. & ABEDI, J. 2011 The effect of anisotropic dispersion on the convective mixing in long-term CO_2 storage in saline aquifers. *AIChE J.* **57** (3), 561–570.

HESSE, M. A., TCHELEPI, H. A. & ORR, F. M. 2006 Natural convection during aquifer CO_2 storage *GHGT-8, 8th International Conference on Greenhouse Gas Control Technologies, Trondheim, Norway*.

HEWITT, D. R., NEUFELD, J. A. & LISTER, J. R. 2013 Convective shutdown in a porous medium at high Rayleigh number. *J. Fluid Mech.* **719**, 551–586.

HIDALGO, J. J., FE, J., CUETO-FELGUEROSO, L. & JUANES, R. 2012 Scaling of convective mixing in porous media. *Phys. Rev. Lett.* **109**, 264503.

HOLLOWAY, S. & SAVAGE, D. 1993 The potential for aquifer disposal of carbon-dioxide in the UK. *Energy Convers. Manage.* **9** (11), 925–932.

IPCC, 2005 *Special Report on Carbon Dioxide Capture and Storage* (ed. B. Metz, O. Davidson, H. de Coninck, M. Loos & L. Meyer), Cambridge University Press.

KNEAFSEY, T. J. & PRUESS, K. 2010 Laboratory flow experiments for visualizing carbon dioxide-induced, density-driven brine convection. *Trans. Porous Med.* **82**, 123–139.

KOLMOGOROV, A. N. 1941 The local structure of turbulence in incompressible viscous fluid for very large Reynolds number. *C. R. Dokl. Acad. Sci. URSS* **30**, 301–305.

KOLMOGOROV, A. N. 1962 A refinement of previous hypotheses concerning the local structure of turbulence in a viscous incompressible fluid at high Reynolds number. *J. Fluid Mech.* **13**, 82–85.

LAKE, L. 1989 *Enhanced Oil Recovery*. Prentice Hall.

LINDEBERG, E. & BERGMO, P. 2003 The long-term fate of CO_2 injected into an aquifer. In *Greenhouse Gas Control Technologies* (ed. J. Gale & Y. Kaya), vol. 1, pp. 489–495. Elsevier Science Ltd.

MACMINN, C. W., SZULCZEWSKI, M. L. & JUANES, R. 2011 CO_2 migration in saline aquifers. Part 2. Capillary and solubility trapping. *J. Fluid Mech.* **688**, 321–351.

Downloaded from https://www.cambridge.org/core. University of Basel Library, on 30 May 2017 at 17:27:58, subject to the Cambridge Core terms of use, available at https://www.cambridge.org/core/terms. https://doi.org/10.1017/jfm.2014.229

NEUFELD, J. A., HESSE, M. A., RIAZ, A., HALLWORTH, M. A., TCHELEPI, H. A. & HUPPERT, H. E. 2010 Convective dissolution of carbon dioxide in saline aquifers. *Geophys. Res. Lett.* **37** (22), L22404.

PAU, G., BELL, J. B., PRUESS, K., ALMGREN, A. S., LIJEWSKI, M. J. & ZHANG, K. 2010 High-resolution simulation and characterization of density-driven flow in CO_2 storage in saline aquifers. *Adv. Water Resour.* **33**, 443–455.

POPE, S. B. 2000 *Turbulent Flows*. Cambridge University Press.

PRUESS, K. & NORDBOTTEN, J. 2011 Numerical simulation studies of the long-term evolution of a CO_2 plume in a saline aquifer with a sloping caprock. *Trans. Porous Med.* **90**, 135–151.

RIAZ, A., HESSE, M., TCHELEPI, H. A. & ORR, F. M. 2006 Onset of convection in a gravitationally unstable diffusive boundary layer in porous media. *J. Fluid Mech.* **548**, 87–111.

RICHARDSON, L. F. 1922 *Weather Prediction by Numerical Process*. Cambridge University Press, (reprint: Dover, New York 1965).

SLIM, A. C., BANDI, M. M., MILLER, J. C. & MAHADEVAN, L. 2013 Dissolution-driven convection in a Hele-Shaw cell. *Phys. Fluids* **25** (2), 024101.

SMAGORINSKY, J. 1963 General circulation experiments with the primitive equations: I. The basic experiment. *Mon. Weath. Rev.* **91**, 99–152.

YANG, C. D. & GU, Y. G. 2006 Accelerated mass transfer of CO_2 in reservoir brine due to density driven natural convection at high pressures and elevated temperatures. *Ind. Engng Chem. Res.* **45** (8), 2430–2436.

YANG, Z. M. & YORTSOS, Y. C. 1997 Asymptotic solutions of miscible displacements in geometries of large aspect ratio. *Phys. Fluids* **9** (2), 286–298.

YORTSOS, Y. 1995 A theoretical-analysis of vertical flow equilibrium. *Trans. Porous Med.* **18** (2), 107–129.

Downloaded from https://www.cambridge.org/core. University of Basel Library, on 30 May 2017 at 17:27:58, subject to the Cambridge Core terms of use, available at https://www.cambridge.org/core/terms. https://doi.org/10.1017/jfm.2014.229